Check for updates

Electroless deposition of RuO_2-based nanoparticles for energy conversion applications†

Jing-Mei Li, [ID] *[ab] Chi-Chang Hu, [ID] *[a] Tzu-Ho Wu[a] and Yung-Jung Hsu [ID] [b]

This study reports a delicate electroless approach for the deposition of $RuO_2 \cdot nH_2O$ nanoparticles on the $VO_x \cdot mH_2O$ nanowires and this method can be extended to deposit $RuO_2 \cdot nH_2O$ nanoparticles on various material surfaces. Electrochemical characterizations, including linear sweep voltammetry (LSV), electrochemical quartz crystal microbalance (QCM) analysis and rotating ring-disc electrode (RRDE) voltammetry, were carried out to investigate the growth mechanism. The deposition involves the catalytic reduction of dissolved oxygen by the V^{4+} species of $VO_x \cdot mH_2O$, which drives the oxidation of $RuCl_3$ to proceed with the growth of $RuO_2 \cdot nH_2O$. This core/shell $VO_x \cdot mH_2O/RuO_2 \cdot nH_2O$ shows a better catalytic activity of the oxygen reduction reaction (ORR) than $RuO_2 \cdot nH_2O$, which is ascribed to the pronounced dispersion of $RuO_2 \cdot nH_2O$. Such an electroless approach was applicable to the preparation of a RuO_2-based nanoparticle suspension as well as the deposition of nanocrystalline $RuO_2 \cdot nH_2O$ on other functional supports like TiO_2 nanowires. The thus-obtained RuO_2-decorated TiO_2 nanorods exhibit significantly an enhanced photoactivity toward photoelectrochemical water oxidation. The versatility of the current electroless approach may facilitate the widespread deployment of nanocrystalline $RuO_2 \cdot nH_2O$ in a variety of energy-related applications.

1. Introduction

With exceptional electrochemical and optoelectronic properties, ruthenium oxide (RuO_2) has garnered considerable attention for numerous technological applications. For example, hydrous ruthenium oxide ($RuO_2 \cdot nH_2O$) is considered to be one of the most promising electrode materials for supercapacitors due to its capability of driving reversible multi-electron transfer redox reactions with over-lapped potentials.[1–5] In electrocatalysis, RuO_2 can function as an active component for chlorine generation from HCl,[6] catalytic CO_2 reduction[7,8] as well as the efficient catalyst for the oxygen and hydrogen evolution reactions.[9–11] Furthermore, promising potentials for photocatalytic water splitting,[12–15] sodium-ion batteries,[16] aerobic oxidation of alcohols,[17] nitrous oxide (N_2O) decomposition,[18] photocatalytic CO_2 reduction,[19] carbon-free H_2 production,[20] and room-temperature CO oxidation[21] have also been demonstrated by exploiting the intrinsic properties of RuO_2. Recently the lithium–oxygen (Li–O_2) battery has attracted tremendous attention and RuO_2 plays a key role as bifunctional catalyst for

the oxygen reduction reaction (ORR) and oxygen evolution reaction (OER) to reduce the overpotential of discharging/charging process.[22–25] However, the high cost of ruthenium precursors has hindered the large-scale deployment of RuO_2. Especially for the bulk, thick RuO_2 films, the relatively low specific capacitance resulting from the long diffusion lengths of ions and electrons has limited their practical applications.[7] Thanks to the appealing attributes derived from the size effect, nanocrystalline RuO_2 with high specific surface area and enhanced kinetics of mass and charge transport can provide a promising solution to address the above issues.[8] Consequently, countless efforts have been dedicated to the preparation of RuO_2 nanostructures with miscellaneous structural forms, *e.g.*, nanoparticles and nanotubes, whose capacitive performance can be accordingly enhanced.

In view of the ease of handling and the feasibility of massive production, nanoparticles of RuO_2 have proven their prowess in energy storage[26,27] and energy conversion applications.[11,28,29] To achieve homogeneous distribution and thereby satisfactory performance, depositing RuO_2 nanoparticles on specific substrates with unique functionalities is desirable.[17,25,30–34] For instance, carbon nanotubes were utilized as the template to grow highly dispersed RuO_2 with the size down to 1.35 nm.[17] With the striking structural uniformity, the resultant composites exhibited high activity and excellent selectivity toward catalytic aerobic oxidation. Moreover, RuO_2 nanoparticles were deposited on TiO_2 nanoflowers to form nanocomposites with three-dimensional porous architectures, which displayed high

[a]*Department of Chemical Engineering, National Tsing Hua University, Hsinchu 30013, Taiwan. E-mail: cchu@che.nthu.edu.tw; maylinli_may@hotmail.com*

[b]*Department of Materials Science and Engineering, National Chiao Tung University, Hsinchu 30010, Taiwan*

† Electronic supplementary information (ESI) available: The concentration of proton at the surface of $VO_x \cdot mH_2O$ *versus* time, XPS spectra of VO_x, precipitate from solution contained $VOSO_4$ and $NiCl_2$, and $NiCl_2$. See DOI: 10.1039/c8ra07810f

power capacitive characteristics relative to the un-supported RuO_2.[30,31] The superiority was ascribed to the porous nature from the nanoflower backbones of TiO_2 and the connected electron pathways endowed by the well distributed RuO_2. Till now, a vast body of the literature has documented various synthetic approaches for the deposition of RuO_2 nanoparticles on functional substrates.[33] Most of them however involved complicated preparation processes, such as prolonged reaction time,[17,34] energy-consuming steps, for example, the need of post-annealing treatment at an elevated temperature,[9,24,35] or the most concerned issue, i.e. the use of large amount of ruthenium precursors,[17,22,23,34] which may further obstruct the practical utilization of nanocrystalline RuO_2. Hence, the creation of a facile, cost-effective approach to obtain highly dispersive RuO_2 with structural integrity is imperative more than ever before.

In this work, we developed a simple yet effective electroless method to deposit $RuO_2 \cdot nH_2O$ nanoparticles on hydrated vanadium oxide ($VO_x \cdot mH_2O$) nanowires. Here, $VO_x \cdot mH_2O$ nanowire arrays were employed as supports for $RuO_2 \cdot nH_2O$ deposition. The nanowire backbones not only provided growth platform for homogeneous distribution of $RuO_2 \cdot nH_2O$ deposits but also formed abundant structural interstices to create three-dimensional porosities, which is beneficial to the applications requiring high surface area and facile charge transport, such as electrochemical energy conversion, solar energy conversion, catalysis and sensing. The deposition was conducted at room temperature and completed within 1 h without the post-heat treatment. The resultant $RuO_2 \cdot nH_2O$ crystallites had an average size of 1.9 nm and were homogeneously distributed on the $VO_x \cdot mH_2O$ nanowire surface with an ultrahigh density of 2.1×10^{13} particles per μm^2. The results of linear sweep voltammetry (LSV), quartz crystal microbalance (QCM) analysis and rotating ring-disc electrode (RRDE) voltammetry suggested that the V^{4+} species of $VO_x \cdot mH_2O$ nanowires catalyzed the reduction of dissolved oxygen, which drove the oxidation of Ru^{3+} to deposit $RuO_2 \cdot nH_2O$. Such a delicate electroless deposition process can be extended for the deposition of nanocrystalline RuO_2 on other oxides supports, for example TiO_2 nanowires, which has significant implications in the development of multi-functional nanocomposites for a variety of energy-related applications ranging from photoelectrochemical energy conversion to electrochemical energy storage.

2.   Materials and methods

2.1.   Preparation of $RuO_2 \cdot nH_2O$-decorated $VO_x \cdot mH_2O$ nanowires

$VO_x \cdot mH_2O$ nanowires were first grown on graphite substrates (1 $\times$ 1 cm) using the anodic deposition method.[36,37] The substrate deposited with $VO_x \cdot mH_2O$ nanowires was then immersed into a reaction solution (50 mL) containing 10 mM of $RuCl_3 \cdot xH_2O$ and 10 mM of CH_3COONa. Upon steady stirring at room temperature for 1 h, $RuO_2 \cdot nH_2O$ nanoparticles were deposited on the $VO_x \cdot mH_2O$ nanowire surface. The substrate was then taken out, rinsed with de-ionized water and dried at room temperature. To study the growth mechanism, the reaction solution of V^{4+} species was used and prepared by adding 0.2 g of

$VOSO_4$ into 50 mL of deionized water. To prepare the reaction solution of V^{5+}, a stoichiometric content of H_2O_2 was added along with 0.2 g of $VOSO_4$ in the 50 mL deionized water, which led to the complete oxidation of V^{4+} to V^{5+}. The homogeneous growth of RuO_2 nanoparticle suspensions was conducted by employing the reaction solution containing 10 mM of $RuCl_3 \cdot xH_2O$, 10 mM of CH_3COONa and a given amount of V^{4+}.

Rutile TiO_2 nanorod arrays were grown on fluorine-doped tin oxide (FTO) glass substrates using a hydrothermal method reported in the literature.[38,39] Concentrated HCl (15 mL) was diluted with deionized water (15 mL) and then mixed with titanium n-butoxide ($Ti(OBu)_4$, 0.5 mL) in a 100 mL beaker. The resulting clear solution was transferred to a Teflon-lined stainless-steel autoclave (40 mL in volume), where a clean FTO glass substrate was submerged into the solution. The sealed autoclave was heated in an electric oven at 150 °C for 5 h and then slowly cooled to room temperature. A white TiO_2 nanorod film was uniformly coated on the FTO glass substrate after cooling. The samples were thoroughly washed with deionized water and then annealed in air at 550 °C for 3 h to improve the crystallinity.

2.2.   Characterizations

The morphology and dimensions of the samples were observed with a field-emission scanning electron microscope (FE-SEM, Hitachi S-4800) and a field-emission transmission electron microscope (FE-TEM, Philips, Tecnai F20 G2). The elemental analysis of the samples was conducted with energy dispersive X-ray spectrometer (EDS), an accessory of TEM. The electrochemical quartz crystal microbalance (EQCM) analysis was performed on a commercially available Au/Ti-sputtered quartz electrode with an electrochemical workstation (CH Instruments, CHI 4051a). The chemical environment information was acquired with an X-ray photoelectron spectrometer (XPS, ULVAC-PHI, Quantera SXM) using Al Kα radiation ($h\nu = 1486.69$ eV) under high vacuum conditions. Electrochemical characterizations were carried out using an electrochemical workstation (CH Instruments, CHI 633A). To study the oxygen reduction reaction (ORR) kinetics, the RRDE voltammetry was employed and the potential values were represented with respect to the reversible hydrogen electrode (RHE). The measurements were conducted at 900 rpm with a scan rate of 5 mV s^{-1}. The photoelectrochemical measurements were performed and in 1.0 M NaOH under a three-electrode configuration where the Ru-based nanoparticles (NPs) decorated TiO_2 nanorods, Pt foil, and Ag/AgCl serve as the working, counter, and reference electrodes, respectively. The simulated sunlight irradiation was produced using a solar simulator (LCS-100 Solar Simulator) with an AM 1.5 global filter with the light intensity of 100 mW cm^{-2}.

3.   Results and discussion

3.1.   Structural investigations

Fig. 1(A) shows the SEM image of $VO_x \cdot mH_2O$ nanowires obtained from the anodic deposition process. These nanowires

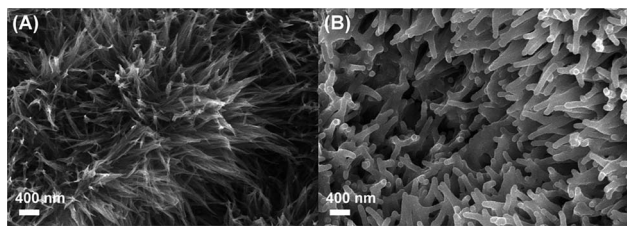**Fig. 1** SEM images of (A) pristine $VO_x \cdot mH_2O$ and (B) $RuO_2 \cdot nH_2O$-decorated $VO_x \cdot mH_2O$ nanowires.

were bundled, mutually interlaced to form porous urchin-like structures. By virtue of this highly porous structural feature, the $VO_x \cdot mH_2O$ nanowires have been demonstrating promising potentials as the cathode of asymmetric Li-ion supercapacitors.[37] After reacted with $RuCl_3$ in the electroless reaction, the nanowires became thicker in diameter and transformed into coral-like structures with rounded ends. As clearly observed in Fig. 1(B), the drastic morphology change indicates that certain deposits should have grown on the nanowire surface.

TEM observations were carried out to examine the microstructural details. As evident in Fig. 2(A), the nanowire surface was covered with a large quantity of nanoparticles. The deposited nanoparticles showed an average size of 1.9 nm and were uniformly distributed on the nanowire surface with an ultrahigh density of 2.1×10^{13} particles per μm^2. The corresponding TEM-EDS elemental maps in Fig. 2(B) verify that the deposited particles were composed of Ru and O, suggesting the formation of Ru oxide-based nanoparticles on the surface of $VO_x \cdot mH_2O$ nanowires.

3.2. Deposition mechanism

To manipulate the present electroless process for depositing Ru oxide-based nanoparticles, it is essential to understand the growth mechanism behind. For electroless deposition of metal oxides in the higher oxidation state in comparison with their precursors (e.g., RuO_2 deposited from $RuCl_3$), oxidizing agents are required to drive the metal ion oxidation. Since no specific oxidant was added in the current synthetic process, the interactions among the reaction species, i.e., $RuCl_3$ precursor,

$VO_x \cdot mH_2O$ electrode, and dissolved oxygen molecules, might be responsible for the initiation of the Ru^{3+} oxidation. We first analyzed the oxidation kinetics of Ru^{3+} with electrochemical characterization methods and evaluated the possible involvement of $VO_x \cdot mH_2O$ electrode. Fig. 3(A) presents the LSV curves for two different electrodes, graphite substrates and $VO_x \cdot mH_2O$ nanowires, recorded in the electrolyte containing $RuCl_3$. For graphite substrate, a prominent anodic peak at 1.15 V vs. Ag/AgCl was noticed, which was attributed to the oxidation of Ru^{3+} into Ru^{4+}. The Ru^{3+} oxidation peak remained eminent for the $VO_x \cdot mH_2O$ nanowires electrode, exhibiting a higher current density with a less positive potential relative to the peak on the graphite substrate. This phenomenon suggests that $VO_x \cdot mH_2O$ nanowires may facilitate the electrochemical oxidation of Ru^{3+} by improving the reaction kinetics. Note that $VO_x \cdot mH_2O$ nanowires were composed of mixed V^{4+} and V^{5+} oxy-hydroxyl species,[36,37] shown in Fig. S1.† To clarify the species responsible for facilitating the oxidation of Ru^{3+}, we carried out the electroless reaction by using the reaction solution of V^{4+} or V^{5+} and compared the results with QCM. Fig. 3(B) displays the mass change of the QCM analyzer for the reaction solutions of V^{4+} and V^{5+}. Also Fig. 3(B) includes the QCM result from the V^{4+} solution with N_2 purging to clarify the possible role of the dissolved oxygen in the electroless deposition of RuO_2. Several important features can be observed from Fig. 3(B). First, the electroless deposition was totally inhibited in the reaction solution of V^{5+}, revealing that V^{4+} was the main species for facilitating the $RuCl_3$ oxidation. Since the composition of $VO_x \cdot mH_2O$ electrode was unchanged during the electroless deposition process, V^{4+} was considered to be a catalyst for $RuCl_3$ oxidation instead of an oxidant agent. Second, the deposition rate was hindered as the reaction solution of V^{4+} was purged with N_2, suggesting that the dissolved oxygen is the oxidizing agent in the catalytic oxidation of $RuCl_3$. Furthermore, when the $RuCl_3$ solution without V^{4+} was purged with air for 1 h or exposed to the ambient air for 7 days, no precipitation could be gathered. Accordingly, we propose that the V^{4+} species of $VO_x \cdot mH_2O$ nanowires catalyze the reduction of dissolved oxygen to drive the oxidation of $RuCl_3$ in order to proceed with the $RuO_2 \cdot nH_2O$ deposition.

To manifest the above oxygen reduction contention, we investigated the electrochemical behavior of $VO_x \cdot mH_2O$

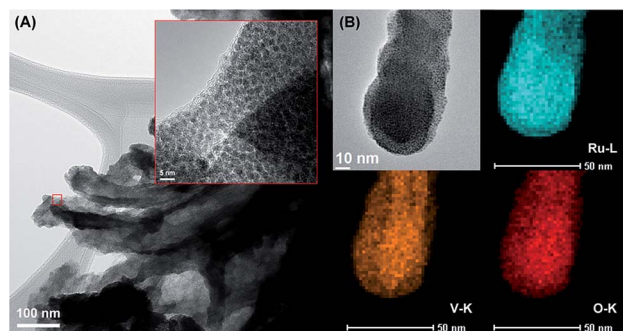**Fig. 2** (A) TEM image and (B) TEM-EDS mapping results of $RuO_2 \cdot nH_2O$-decorated $VO_x \cdot mH_2O$ nanowires. Inset in (A) shows the enlarged image at the marked region.

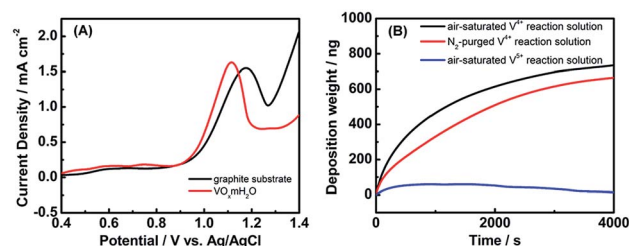**Fig. 3** (A) LSV curves of $RuCl_3$ oxidation for graphite substrates and $VO_x \cdot mH_2O$ nanowires recorded in the reaction solution. (B) QCM mass change on the electrode recorded from the reaction solutions containing V^{4+} and V^{5+}, respectively. The result of performing N_2 purging was also included for comparison.

nanowires toward the ORR. It should be noted that the ORR in aqueous solutions occurs mainly through two pathways: the direct 4-electron reduction pathway from O_2 to H_2O, and the 2-electron reduction pathway from O_2 to H_2O_2.[40] For the 4-electron transfer pathway, the catalytic oxidation of Ru^{3+} was driven by the direct electron transfer from Ru^{3+} to the oxygen molecules adsorbed on the $VO_x \cdot mH_2O$ surface, which generated OH^- ions to enable the growth of $RuO_2 \cdot nH_2O$. As to the two-electron transfer pathway, highly oxidative H_2O_2 could be produced in the vicinity of the $VO_x \cdot mH_2O$ surface, subsequently oxidizing Ru^{3+} to proceed with the $RuO_2 \cdot nH_2O$ deposition.[1,17] Interestingly, the concentration of proton at the surface of $VO_x \cdot mH_2O$ without potential bias was monitored after $RuCl_3$ was added (in Fig. S2†). The result shows that the concentration of proton increased suddenly at first and reached a plateau, which indicates that the ORR and RuO_2 deposition involve hydroxyl ions. Note that both 4-electron and 2-electron pathways of the ORR consume protons under the acidic circumstance to oxidize Ru(III) to form the Ru(IV) ions (i.e., decrease in proton concentration). Since every Ru(IV) ion will react with four OH^- to form $Ru(OH)_4$, which significantly increases the proton

concentration, we cannot determinate the deposition mechanism from the sudden increase in the proton concentration. Accordingly, the RRDE method was employed to give a deep investigation. Fig. 4(A) shows the RRDE voltammograms on the GC electrodes deposited with $VO_x \cdot mH_2O$ in 0.5 M Na_2SO_4 electrolyte with pH = 3, a $RuCl_3$-free electrolyte. When the applied potentials were swept from 0.8 to 0.2 V vs. RHE, the disk current density continuously increased. The apparent electron transfer number (n) can be determined from the equation, $n = \dfrac{4I_D}{I_D + I_R/N}$, where I_D is the disk current, I_R is the ring current, and N is the ring collection coefficient (0.38). As shown in Fig. 4(B), the apparent electron transfer number of ORR varied from 2.6 to 3.9 for the $RuCl_3$-free electrolyte. In fact, the ORR on $VO_x \cdot mH_2O$ in the electrolyte containing $RuCl_3$ was studied as well. However, the result was not shown here because of the enormous possibility of direct reduction of Ru^{3+} into Ru metal according to the ruthenium Pourbaix diagram,[41] which may lead to misunderstanding. The RRDE results manifest that the ORR catalyzed by $VO_x \cdot mH_2O$ is shifted from the 2-electron transfer pathway to the 4-electron transfer pathway with the application of more negative potentials. This phenomenon suggests that without the potential bias, the ORR should obey the 2-electron transfer pathway, resulting in the phenomenon of increasing the proton concentration.

3.3. Applications of the catalytic redox deposition of $RuO_2 \cdot nH_2O/VO_x \cdot mH_2O$

Fig. 4(A) shows the RRDE voltammograms on the GC electrodes deposited with $RuO_2 \cdot nH_2O/VO_x \cdot mH_2O$ and $RuO_2 \cdot nH_2O$ in 0.5 M Na_2SO_4 electrolyte with pH = 3. The onset potentials of the ORR on $RuO_2 \cdot nH_2O/VO_x \cdot mH_2O$ and $RuO_2 \cdot nH_2O$ are about 0.83 and 0.34 V, respectively. Note here that the onset potential of the ORR was defined as the potential where the current density of oxygen reduction reached 0.5 A cm^{-2} g^{-1}. Clearly, the usage of $VO_x \cdot mH_2O$ nanowires as the catalyst backbone promotes the onset potential, probably due to a higher electrolyte-accessible surface area in comparison with $RuO_2 \cdot nH_2O$. Also note that the catalytic activity of $RuO_2 \cdot nH_2O$ is extremely low at potentials positive than 0.4 V while a sharp increase in the disc current density was found in the less positive potential region. This phenomenon may be assigned to that the Ru(III)/Ru(IV) redox couple is the main active species catalyzing the ORR.[42–45] In Fig. 4(B), the mean electron transfer number, n, of $RuO_2 \cdot nH_2O$ monotonously increases from ca. 2.6 to 3.9 with the negative shift in the electrode potential in Fig. 4(B). Surprisingly, the mean electron transfer number of the ORR on $RuO_2 \cdot nH_2O/VO_x \cdot mH_2O$ was approximately constant and very close to 4. This result reveals that $RuO_2 \cdot nH_2O/VO_x \cdot mH_2O$ is an excellent catalyst for the ORR, leading to the four-electron transfer pathway. From all the above results and discussion, the $RuO_2 \cdot nH_2O/VO_x \cdot mH_2O$ composite is a promising electrocatalyst of the ORR for the applications of H_2O_2 generation and fuel cells in weak acid media containing different supporting electrolytes.
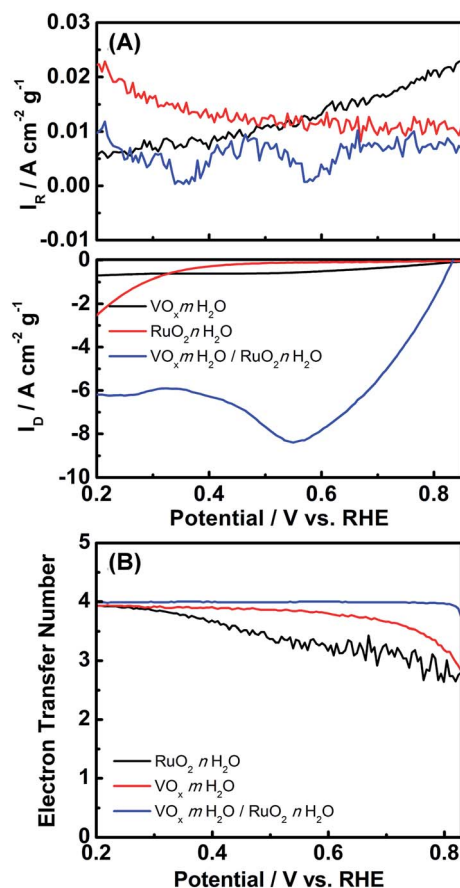

Fig. 4 (A) The RRDE voltammograms and (B) the mean electron transfer number (n) of the ORR obtained from the GC disk electrode deposited with (1) $VO_x \cdot mH_2O/RuO_2 \cdot nH_2O$, (2) $VO_x \cdot mH_2O$, and (3) $RuO_2 \cdot nH_2O$ in O_2-saturated 0.5 M Na_2SO_4 with pH = 3 at 5 mV s^{-1} and a rotating speed of 900 rpm.

3.4. RuO$_2$ suspensions and deposition on TiO$_2$ nanowires

To realize the growth mechanism, we further performed the electroless reaction in a reaction solution simply containing V^{4+} species and the RuCl$_3$ precursor. The synthesis was conducted under the ambient atmosphere for 6 h, which produced abundant nanoparticle suspensions in the bulk solution. The morphology and composition of resultant RuO$_2$ precipitates were characterized with SEM and XPS analyses. The SEM image in Fig. 5(A) shows that the precipitates are particles of 100–200 nm in size. From a detailed examination, these particles are considered to be aggregates of tiny nanocrystals with sizes of 50–80 nm. The corresponding XPS spectrum in Fig. 5(B) suggests the diverse chemical environment of ruthenium species within the precipitates. The deconvolution of Ru 3p peak yields three chemical states, RuO$_2$, RuO$_2 \cdot n$H$_2$O, and Ru(OH)$_3$, with the percentage determined to be 37.8, 40.6, and 21.6 at%, respectively. This illustration highlights the versatility of our electroless approach which not only deposits RuO$_2 \cdot n$H$_2$O nanoparticles on the VO$_x \cdot m$H$_2$O nanowires but also produces RuO$_2$-based nanoparticle suspensions in the bulk solution.

The feasibility in obtaining the highly dispersive and well suspending nanocrystalline RuO$_2$ is particularly appealing for stimulating the practical applications. As a demonstration, TiO$_2$ nanowires array was utilized as a frame in the electroless deposition of nanocrystalline RuO$_2$. Here the high-resolution TEM image was employed to inspect the dispersion of RuO$_2$ on the surface of TiO$_2$ nanowires and Fig. 6 shows that TiO$_2$ nanowire was covered with a 2 nm thin layer of nanocrystalline RuO$_2$ to form a core/shell nanostructure. The lattice fringes of TiO$_2$ frame with the interplanar spacing of 0.32 nm and 0.29 nm were observed, consistent with the d-spacing of (110) and (001) planes of rutile TiO$_2$.[38] On the other hand, the lattice fringes of RuO$_2$ nanoparticles with the interplanar spacing of 0.221 nm and 0.225 nm were obtained, corresponding to the d-spacing of (111) and (200) planes of rutile RuO$_2$, respectively.

The capacitive behavior of TiO$_2$ nanowires and TiO$_2$/RuO$_2$ core/shell structure was examined. For the comparison purpose, the electroless deposition of nanocrystalline RuO$_2$ on an FTO was conducted as well. From a comparison of CV curves of the core/shell TiO$_2$/RuO$_2$ and RuO$_2$-decorated FTO in Fig. 7(A), well-dispersed RuO$_2$ nanocrystallites promotes the utilization of active species, leading to higher specific capacitance of the core/shell TiO$_2$/RuO$_2$ in comparison with the RuO$_2$-decorated FTO electrode. Since RuO$_2$ has been widely
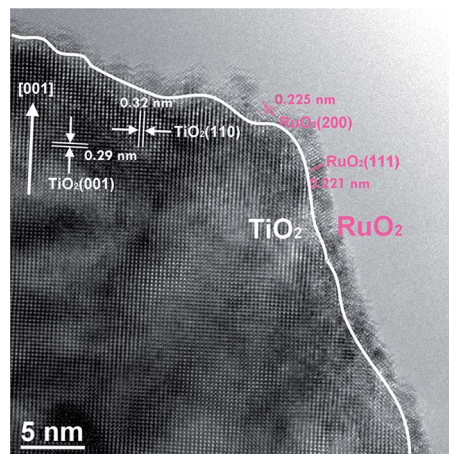
recognized as an efficient oxygen evolution co-catalyst in photoelectrochemical water splitting,[46,47] the decoration of RuO$_2$ nanocrystallites onto TiO$_2$ may significantly enhance the photocatalytic activity of TiO$_2$ for water oxidation. Here, the photoelectrochemical measurements were conducted to evaluate the potential of the RuO$_2$-decorated TiO$_2$ nanowire for water splitting. Fig. 7(B) compares the LSV curves of pristine TiO$_2$ and RuO$_2$-decorated TiO$_2$ photoelectrodes for water oxidation. Evidently, RuO$_2$-decorated TiO$_2$ displays larger photocurrent densities in the entire potential widow than pristine TiO$_2$. This phenomenon was ascribed to the improved water oxidation kinetics on the decorated RuO$_2$.

To extend the application of this electroless deposition, NiCl$_2$ was used as the precursor for Ni-based oxyhydroxide deposition and a precipitate was observed from the mixed solution of VOSO$_4$ and NiCl$_2$. In comparison with the precursor NiCl$_2$, the precipitate displayed different Ni 2p spectrum shown in Fig. S3.† Ni 2p$_{3/2}$ was further deconvoluted into two peaks cantered at 856.5 eV and 857.6 eV shown in Fig. S4,† which are corresponding to Ni(OH)$_2$ and NiOOH.[48] Again, this result demonstrates the oxidation of NiCl$_2$ to form nickel oxyhydroxide and nickel hydroxide. Based on the above preliminary test, this V^{4+}-catalyzed electroless deposition presents an enormous potential in transition metal oxide deposition.
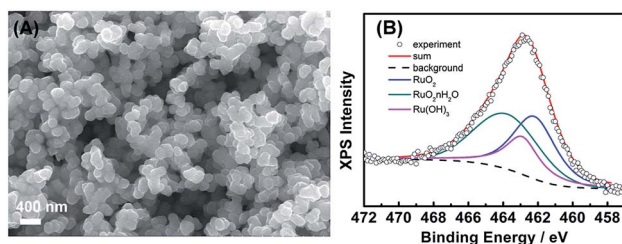

Fig. 6 A high-resolution TEM image of a RuO$_2$-decorated TiO$_2$ nanowire.

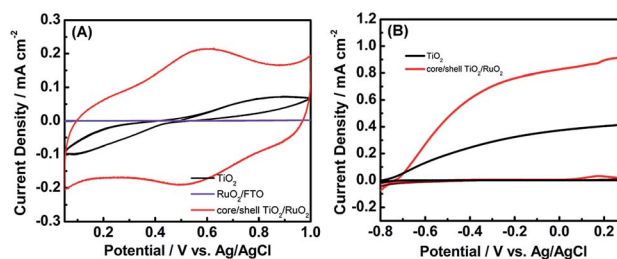Fig. 5 (A) SEM images and (B) XPS Ru 3p core-level spectra of RuO$_2$-based nanoparticle suspensions.

Fig. 7 (A) CV curves of pristine TiO$_2$ and RuO$_2$-decorated TiO$_2$ for supercapacitors. (B) LSV curves of pristine TiO$_2$ and RuO$_2$-decorated TiO$_2$ photoanodes for water oxidation.

4. Conclusions

An effective electroless approach has been developed for the deposition of nanocrystalline RuO_2 onto various functional supports such as $VO_x \cdot mH_2O$ and TiO_2 nanowires as well as the preparation of RuO_2-based nanoparticle suspensions in the bulk solution. The success of this synthetic approach relied on the presence of V^{4+} species which catalyzed the oxygen reduction reaction to drive $RuCl_3$ oxidation for RuO_2 deposition. The versatility of the present electroless approach shall foster the advanced applications of nanocrystalline RuO_2 in a wide array of fields, which include electrochemical cells, room-temperature CO oxidation, and photocatalytic water splitting.

Conflicts of interest

There are no conflicts to declare.

Acknowledgements

References

1 K.-H. Chang and C.-C. Hu, *J. Electrochem. Soc.*, 2004, **151**, A958–A964.

2 C.-C. Hu, K.-H. Chang, M.-C. Lin and Y.-T. Wu, *Nano Lett.*, 2006, **6**, 2690–2695.

3 C.-C. Hu, M.-J. Liu and K.-H. Chang, *J. Power Sources*, 2007, **163**, 1126–1131.

4 I. L. Chen, Y.-C. Wei, T.-Y. Chen, C.-C. Hu and T.-L. Lin, *J. Power Sources*, 2014, **268**, 430–438.

5 I. L. Chen, T.-Y. Chen, Y.-C. Wei, C.-C. Hu and T.-L. Lin, *Nanoscale*, 2014, **6**, 2861–2871.

6 D. Teschner, R. Farra, L. Yao, R. Schlögl, H. Soerijanto, R. Schomäcker, T. Schmidt, L. Szentmiklósi, A. P. Amrute, C. Mondelli, J. Pérez-Ramírez, G. Novell-Leruth and N. López, *J. Catal.*, 2012, **285**, 273–284.

7 M. Karamad, H. A. Hansen, J. Rossmeisl and J. K. Nørskov, *ACS Catal.*, 2015, **5**, 4075–4081.

8 J. Qu, X. Zhang, Y. Wang and C. Xie, *Electrochim. Acta*, 2005, **50**, 3576–3580.

9 L. M. Torres-Martínez, R. Gómez, O. Vázquez-Cuchillo, I. Juárez-Ramírez, A. Cruz-López and F. J. Alejandre-Sandoval, *Catal. Commun.*, 2010, **12**, 268–272.

10 Y. Lee, J. Suntivich, K. J. May, E. E. Perry and Y. Shao-Horn, *J. Phys. Chem. Lett.*, 2012, **3**, 399–404.

11 C. Gómez-Solís, J. C. Ballesteros, L. M. Torres-Martínez and I. Juárez-Ramírez, *Fuel*, 2016, **166**, 36–41.

12 K. Ikarashi, J. Sato, H. Kobayashi, N. Saito, H. Nishiyama and Y. Inoue, *J. Phys. Chem. B*, 2002, **106**, 9048–9053.

13 S. D. Tilley, M. Schreier, J. Azevedo, M. Stefik and M. Graetzel, *Adv. Funct. Mater.*, 2014, **24**, 303–311.

14 J. Park, J. W. Lee, B. U. Ye, S. H. Chun, S. H. Joo, H. Park, H. Lee, H. Y. Jeong, M. H. Kim and J. M. Baik, *Sci. Rep.*, 2015, **5**, 11933.

15 M. T. Uddin, O. Babot, L. Thomas, C. Olivier, M. Redaelli, M. D'Arienzo, F. Morazzoni, W. Jaegermann, N. Rockstroh, H. Junge and T. Toupance, *J. Phys. Chem. C*, 2015, **119**, 7006–7015.

16 M. Peng, B. Li, H. Yan, D. Zhang, X. Wang, D. Xia and G. Guo, *Angew. Chem., Int. Ed.*, 2015, **54**, 6452–6456.

17 X. Fu, H. Yu, F. Peng, H. Wang and Y. Qian, *Appl. Catal., A*, 2007, **321**, 190–197.

18 Q. Lin, Y. Huang, Y. Wang, L. Li, X. Y. Liu, F. Lv, A. Wang, W.-C. Li and T. Zhang, *J. Mater. Chem. A*, 2014, **2**, 5178–5181.

19 Q. Liu, Y. Zhou, J. Kou, X. Chen, Z. Tian, J. Gao, S. Yan and Z. Zou, *J. Am. Chem. Soc.*, 2010, **132**, 14385–14387.

20 K. Nagaoka, T. Eboshi, Y. Takeishi, R. Tasaki, K. Honda, K. Imamura and K. Sato, *Sci. Adv.*, 2017, **3**, e1602747.

21 Y. Jiao, H. Jiang and F. Chen, *ACS Catal.*, 2014, **4**, 2249–2257.

22 E. Yilmaz, C. Yogi, K. Yamanaka, T. Ohta and H. R. Byon, *Nano Lett.*, 2013, **13**, 4679–4684.

23 Z. Jian, P. Liu, F. Li, P. He, X. Guo, M. Chen and H. Zhou, *Angew. Chem., Int. Ed.*, 2014, **53**, 442–446.

24 X. Guo, P. Liu, J. Han, Y. Ito, A. Hirata, T. Fujita and M. Chen, *Adv. Mater.*, 2015, **27**, 6137–6143.

25 K. R. Yoon, G. Y. Lee, J.-W. Jung, N.-H. Kim, S. O. Kim and I.-D. Kim, *Nano Lett.*, 2016, **16**, 2076–2083.

26 X. Chuan, C. Wei, W. Xianbin, M. N. Hedhili, W. Nini and H. N. Alshareef, *Adv. Energy Mater.*, 2015, **5**, 1401805.

27 H. Ma, D. Kong, Y. Xu, X. Xie, Y. Tao, Z. Xiao, W. Lv, H. D. Jang, J. Huang and Q.-H. Yang, *Small*, 2017, **13**, 1701026.

28 F. Li, D.-M. Tang, T. Zhang, K. Liao, P. He, D. Golberg, A. Yamada and H. Zhou, *Adv. Energy Mater.*, 2015, **5**, 1500294.

29 X. Paquez, G. Amiard, G. de Combarieu, C. Boissière and D. Grosso, *Chem. Mater.*, 2015, **27**, 2711–2717.

30 C.-C. Hu, H.-Y. Guo, K.-H. Chang and C.-C. Huang, *Electrochem. Commun.*, 2009, **11**, 1631–1634.

31 C.-C. Hu, Y.-L. Yang and T.-C. Lee, *Electrochem. Solid-State Lett.*, 2010, **13**, A173–A176.

32 A. P. Seitsonen and H. Over, *J. Phys. Chem. C*, 2010, **114**, 22624–22629.

33 Y. S. Min, E. J. Bae, K. S. Jeong, Y. J. Cho, J. H. Lee, W. B. Choi and G. S. Park, *Adv. Mater.*, 2003, **15**, 1019–1022.

34 H. Yu, Y. Wu, F. Peng, Y. Zhang, H. Wang and J. Yang, *Catal. Lett.*, 2012, **142**, 100–107.

35 D. A. Neamen, *Semiconductor Physics And Devices*, McGraw-Hill, 2003.

36 J.-M. Li, K.-H. Chang and C.-C. Hu, *Electrochim. Acta*, 2010, **55**, 8600–8605.

37 J.-M. Li, K.-H. Chang and C.-C. Hu, *Electrochem. Commun.*, 2010, **12**, 1800–1803.

38 G. Wang, H. Wang, Y. Ling, Y. Tang, X. Yang, R. C. Fitzmorris, C. Wang, J. Z. Zhang and Y. Li, *Nano Lett.*, 2011, **11**, 3026–3033.

39 Y.-C. Pu, G. Wang, K.-D. Chang, Y. Ling, Y.-K. Lin, B. C. Fitzmorris, C.-M. Liu, X. Lu, Y. Tong, J. Z. Zhang, Y.-J. Hsu and Y. Li, *Nano Lett.*, 2013, **13**, 3817–3823.

40 R. Zhou, Y. Zheng, M. Jaroniec and S.-Z. Qiao, *ACS Catal.*, 2016, **6**, 4720–4728.

41 Y. Sugawara, A. P. Yadav, A. Nishikata and T. Tsuru, *J. Electrochem. Soc.*, 2008, **155**, B897–B902.

42 F. Schlottig, J. Schreckenbach and G. Marx, *Fresenius. J. Anal. Chem.*, 1999, **363**, 209–211.

43 J. W. Long, R. M. Stroud, K. E. Swider-Lyons and D. R. Rolison, *J. Phys. Chem. B*, 2000, **104**, 9772–9776.

44 A. Yamada and J. B. Goodenough, *J. Electrochem. Soc.*, 1998, **145**, 737–743.

45 J.-M. Zen, A. S. Kumar and J.-C. Chen, *J. Mol. Catal. A: Chem.*, 2001, **165**, 177–188.

46 R. Srivastava and P. Strasser, *ECS Trans.*, 2009, **25**, 565–571.

47 H. Suzuki, S. Nitta, O. Tomita, M. Higashi and R. Abe, *ACS Catal.*, 2017, **7**, 4336–4343.

48 N. Watanabe, T. Arakawa, Y. Sasaki, T. Yamashita and I. Koiwa, *J. Electrochem. Soc.*, 2012, **159**, A1949–A1953.